

Refractive index tomography of turbid media by bifocal optical coherence refractometry

Andrei V. Zvyagin*, K. K. M. B. Dilusha Silva, Sergey A. Alexandrov,
Timothy R. Hillman, Julian J. Armstrong

Optical + Biomedical Engineering Laboratory, School of Electrical, Electronic & Computer Engineering,
The University of Western Australia, 35 Stirling Highway, Crawley, Western Australia 6009, Australia

*Now with Physics Department, School of Physical Sciences, The University of Queensland, Brisbane, QLD 4072,
Australia

Takuya Tsuzuki

Advanced Nano Technologies Pty Ltd, 112 Radium Street, Welshpool, Western Australia 6106, Australia

David D. Sampson

Optical and Biomedical Engineering Laboratory, School of Electrical, Electronic & Computer Engineering,
The University of Western Australia, 35 Stirling Highway, Crawley, Western Australia 6009, Australia

dsampson@ee.uwa.edu.au

Abstract: We demonstrate tomographic imaging of the refractive index of turbid media using bifocal optical coherence refractometry (BOCR). The technique, which is a variant of optical coherence tomography, is based on the measurement of the optical pathlength difference between two foci simultaneously present in a medium of interest. We describe a new method to axially shift the bifocal optical pathlength that avoids the need to physically relocate the objective lens or the sample during an axial scan, and present an experimental realization based on an adaptive liquid-crystal lens. We present experimental results, including video clips, which demonstrate refractive index tomography of a range of turbid liquid phantoms, as well as of human skin *in vivo*.

©2003 Optical Society of America

OCIS codes: (110.4500) Optical coherence tomography; (120.5710) Refraction; (180.1790) Confocal microscopy; (170.7050) Turbid media; (170.4580) Optical diagnostics for medicine.

References and links

1. V. V. Tuchin, ed., *Tissue Optics* (SPIE Press, Washington, USA, 2000), Chap. 1.
2. A. Knüttel, S. Bonev, C. Kugler, "In vivo evaluation of locally mapped refractive indices with OCT," in *Progress in Biomedical Optics and Imaging*, V. V. Tuchin et al., eds., Proc. SPIE **4251**, 136-143 (2001).
3. V. V. Tuchin, "Optical and thermal properties of biological tissue" in *Laser-induced interstitial thermotherapy*, G. Müller, A. Roggan, eds. (SPIE Press, Bellingham, USA, 1995).
4. J. F. Koretz and C. A. Cook, "Aging of the optics of the human eye: Lens refraction models and principal plane locations," *Optom. Vision Sci.* **78**, 396-404 (2001).
5. B. B. Das, F. Liu, R. R. Alfano, "Time-resolved fluorescence and photon migration studies in biomedical and random media," *Rep. Prog. Phys.* **60**, 227-292 (1997).
6. S. A. Boppart, B. E. Bouma, C. Pitris, J. F. Southern, M. E. Brezinski, J. G. Fujimoto, "In vivo cellular optical coherence tomography imaging," *Nat. Med.* **4**, 861 (1998).
7. R. Drezek, A. Dunn, R. Richards-Kortum, "Light scattering from cells: finite-difference time-domain simulations and goniometric measurements," *Appl. Opt.* **38**, 3651-3661 (1999).
8. R. S. Gurjar, V. Backman, L. T. Perelman, I. Georgakoudi, K. Badizadegan, I. Itzkan, R. R. Dasari, M. S. Feld, "Imaging human epithelial properties with polarized light-scattering spectroscopy," *Nat. Med.* **7**, 1245 (2002).
9. Y. Domankevitz, J. Waldman, C. P. Lin, R. R. Anderson, "Selective delivery of laser energy to biological tissue based on refractive-index differences," *Opt. Lett.* **25**, 1104-1106 (2000).
10. R. S. Longhurst, *Geometrical and Physical Optics* (Longman, London, 1973) Chap. 5.

11. H. Li and S. Xie, "Measurement method of the refractive index of biotissue by total internal reflection," *Appl. Opt.* **35**, 1793-1795 (1996).
12. F. P. Bolin, L. E. Preuss, R. C. Taylor, R. J. Ference, "Refractive index of some mammalian tissues using a fiber optic cladding method," *Appl. Opt.* **28**, 2297-2303 (1989).
13. W. V. Sorin and D. F. Gray, "Simultaneous thickness and group index measurement using optical low-coherence refractometry," *IEEE Photon. Technol. Lett.* **4**, 105-107 (1992).
14. G. J. Tearney, M. E. Brezinski, J. F. Southern, B.E. Bouma, M. R. Hee, J. G. Fujimoto, "Determination of the refractive index of highly scattering human tissue by optical coherence tomography," *Opt. Lett.* **20**, 2258-2260 (1995).
15. A. Knüttel and M. Boehlau-Godau, "Spatially confined and temporally resolved refractive index and scattering evaluation in human skin performed with optical coherence tomography," *J. Biomed. Opt.* **5**, 83-92 (2000).
16. X. Wang, C. Zhang, L. Zhang, L. Xue, J. Tian, "Simultaneous refractive index and thickness measurements of bio tissue by optical coherence tomography," *J. Biomed. Opt.* **7**, 628-632 (2002).
17. M. Ohmi, Y. Ohnishi, K. Yoden, M. Haruna, "*In vitro* simultaneous measurement of refractive index and thickness of biological tissue by the low coherence interferometry," *IEEE Trans. Biomed. Eng.* **47**, 1266-1270 (2000).
18. A. M. Zysk, J. J. Reynolds, D. L. Marks, P. S. Carney, S. A. Boppart, "Projected index computed tomography," *Opt. Lett.* **28**, 701-703 (2003).
19. S. A. Alexandrov, A. V. Zvyagin, K. K. M. B. D. Silva, D. D. Sampson, "Bifocal optical coherence refractometry of turbid media," *Opt. Lett.* **28**, 117-119 (2003).
20. A. F. Naumov, M. Yu. Loktev, I. R. Guralnik, G. Vdovin, "Liquid crystal adaptive lens with modal control," *Opt. Lett.* **23**, 992-994 (1998).
21. J. M. Schmitt, M. Yadlowsky, R. F. Bonner, "Subsurface imaging of living skin with optical coherence tomography," *Dermatol.* **191**, 93-98 (1995).
22. J. A. Izatt, M. D. Kulkarni, H.-W. Wang, K. Kobayashi, M. V. Sivak, "Optical coherence tomography and microscopy in gastrointestinal tissues," *IEEE J. Selected Top. Quantum Electron.* **2**, 1017-1028 (1996).
23. A. V. Zvyagin, E. D. J. Smith, D. D. Sampson, "Delay and dispersion characteristics of a frequency-domain optical delay line for scanning interferometry," *J. Opt. Soc. Am. A* **20**, 333-341 (2003).
24. M. Kohl, M. Essenpreis, M. Cope, "The influence of glucose concentration upon the transport of light in tissue-simulating phantoms," *Phys. Med. Biol.* **40**, 1267-1287 (1995).
25. J. J. Armstrong, M. S. Leigh, I. D. Walton, A. V. Zvyagin, S. A. Alexandrov, S. Schwer, D. D. Sampson, D. R. Hillman, P. R. Eastwood, "*In vivo* size and shape measurement of large hollow organs using endoscopic long-range optical coherence tomography," *Opt. Express* **11**, 1817-1826 (2003), <http://www.opticsexpress.org/abstract.cfm?URI=OPEX-11-15-1817>.
26. P. G. McCormick, T. Tsuzuki, J. S. Robinson, J. Ding, "Nanoparticle synthesis by mechanochemical processing," *Adv. Mater.* **13**, 1008-1010 (2001).
27. X. W. Suna and H. S. Kwok, "Optical properties of epitaxially grown zinc oxide films on sapphire by pulsed laser deposition," *J. Appl. Phys.* **86**, 408-411 (1999).
28. P. Cooper, "Refractive-index measurements of paraffin, a silicone elastomer, and an epoxy resin over the 500-1500 nm spectral range," *Appl. Opt.* **21**, 3413-3415 (1982).
29. G. J. Tearney and B. E. Bouma, "Atherosclerotic plaque characterization by spatial and temporal speckle pattern analysis," *Opt. Lett.* **27**, 533-535 (2002).
30. Sucrose conversion table, U.S. Dept. Agriculture, File code 135-A-50 (1981).
31. P. J. Caspers, G. W. Lucassen, E. A. Carter, H. A. Bruining, G. J. Puppels, "*In vivo* confocal Raman microspectroscopy of the skin: noninvasive determination of molecular concentration profiles," *J. Invest. Dermatol.* **116**, 434-442 (2001).
32. J. F. de Boer, T. E. Milner, J. S. Nelson, "Determination of the depth-resolved Stokes parameters of light backscattered from turbid media by use of polarization-sensitive optical coherence tomography," *Opt. Lett.* **24**, 300-302 (1999).

1. Introduction

The *in situ* refractive index of living tissue is a key parameter in many biomedical applications of light. Tissue refractive index is important in determining scattering properties and image contrast and as such it is a vital input into models of light-tissue interaction, as well as an important indicator of tissue state.

Models usually rely on tabulated values of refractive index, which have often been measured using a wide variety of methods and under a wide range of conditions. Variations exist in: the state of the tissue - *in vivo*, *in vitro*, frozen, or fixed; the spatial resolution of the measurement, from macroscopic to sub-cellular; and in the wavelength range covered. Thus,

the available data on the refractive index of tissues is fragmentary, often controversial and potentially inaccurate [1].

As an indicator on a macroscopic, morphological level, the refractive index of tissue has been shown to be sensitive to variations in hydration [2], calcification [3], age [4], and tumour malignancy [5]. On a cellular level, the refractive index has been shown to be sensitive to nuclear changes occurring as a result of cell mitosis [6], application of a contrast agent [7], and dysplasia [8]. Refractive index differences have also been exploited in the selective delivery of laser energy to tissue [9].

The most common means of determining the refractive index of a sample is the critical angle method, which is commonly implemented in the form of an Abbe refractometer [10]. The method has been applied to *in vitro* tissue samples [11] but it is not well suited to the determination of the *in situ* refractive index of living tissue. Tissue is a turbid medium of significant optical depth and it and its constituents are in constant motion, which imparts an upper limit on measurement time. The critical angle method is generally too slow, requires clear media, and probes only superficial layers. A related method, in which the sample forms the cladding of an optical fiber, has been used to measure the refractive index of homogenized tissue *in vitro* [12]. The requirements for immersion of the core into a homogeneous medium and access to the distal end of the fiber, as well as the very shallow evanescent penetration, make its use in *in vivo* applications problematic.

The other broad class of methods of refractive-index measurement employs interferometry [13-19]. This class relies on the measurement of the reference-arm optical pathlength required to match the variations in the sample-arm optical pathlength, and must include a means of decoupling the refractive index and the physical length, the product of which gives the optical pathlength. The most straightforward interferometric method of determining the refractive index and the thickness of a sample is to measure the sample arm optical pathlength with and without the sample present [13], but the method is generally not applicable *in vivo*. Tearney *et al.* [14] introduced a suitable focus-tracking method that uses optical coherence tomography (OCT) to track the focal-length shift that results from translating the focus of an objective along the optical axis within a medium. They used it to determine the refractive index of skin tissue *in vivo* and it has been further developed by others for application to tissue [15-17]. The method is inherently somewhat time consuming, as it relies on a sequence of measurements at each discrete axial displacement of focus and, therefore, is prone to sample motion artefacts. Methods based on low-coherence interferometry have shown, in general, the ability to penetrate deeply into turbid and layered tissues, although only with sufficient spatial resolution to determine the average refractive index of tissue layers comprising many cells [2,14,15]. To date, no methods have been shown capable of producing refractive-index tomograms of dynamic processes in tissue occurring on second or sub-second time scales such as arise in laser treatments, for example.

It is apparent that there remains scope for an improved means of accurate, spatially-resolved, motion-artefact-free measurement of refractive index of tissue *in vivo*. With this goal in mind, we have recently proposed a new method, which we have termed bifocal optical coherence refractometry (BOCR) [19]. The method is based on the simultaneous creation of two confocal gates and associated foci within the sample. OCT is used to determine the optical pathlength between the two foci, from which the refractive index is determined. The ultimate limits on the acquisition rate and the resolution of the measurement are the same as those of OCT, which suggests that the method could eventually be used to perform rapid (of the order of milliseconds per image pixel) measurement of the refractive index of tissue *in vivo*.

In this paper, we investigate the use of BOCR for tomographic imaging of refractive index. We describe a new method to vary the bifocal optical pathlength that avoids the need to physically relocate the objective lens or the sample during an axial scan. We present an experimental realization based on a tunable-focal-length liquid-crystal lens. Although the experimental realization is currently too slow, the method shows great potential for *in vivo* applications. We examine homogenous and two-layer tissue phantoms of various types which

demonstrate the feasibility of our method to produce refractive-index tomograms, as well as to monitor variations in the refractive index of turbid media. We also demonstrate the capacity of our method to produce a refractive-index tomogram of thick human stratum corneum *in vivo*.

The paper is organized as follows. In Section 2, we outline the theory behind BOCR. In Section 3, we present an experimental realization and describe the calibration and measurement procedures, as well as the samples used and their preparation. In Section 4, we present experimental results with accompanying discussion and finally draw some conclusions in Section 5.

2. Theory

BOCR is based on a scanning Michelson interferometer illuminated by a linearly-polarized broadband source, as illustrated schematically in Fig. 1, which shows the main optical circuit in optical fiber for convenience. To achieve a bifocus in the sample arm, the beam is collimated, expanded, and passed through an adaptive liquid-crystal lens, LC. The liquid-crystal lens causes a weak convergence of the component of the beam polarized along its slow axis (in the plane of Fig. 1), whereas, the shape of the wavefront of the orthogonal polarization component of the beam is unchanged [20]. An objective lens, L_{obj} , focuses the convergent beam closer to the objective than the collimated beam and, thus, two axially separated foci are formed. Light backscattered from the sample is collected by the optical fiber, thus, producing a confocal gate for each beam. The orientation of the plane of polarization of the beam with respect to the slow axis of the liquid-crystal lens allows control over the light intensity distribution between the two foci. In addition, the liquid-crystal lens permits control over the separation between the two foci through the electronic adjustment of its lens power. The galvanometer-based tiltable mirror, GM, in combination with the objective lens enables lateral scanning of the two confocal gates across the sample.

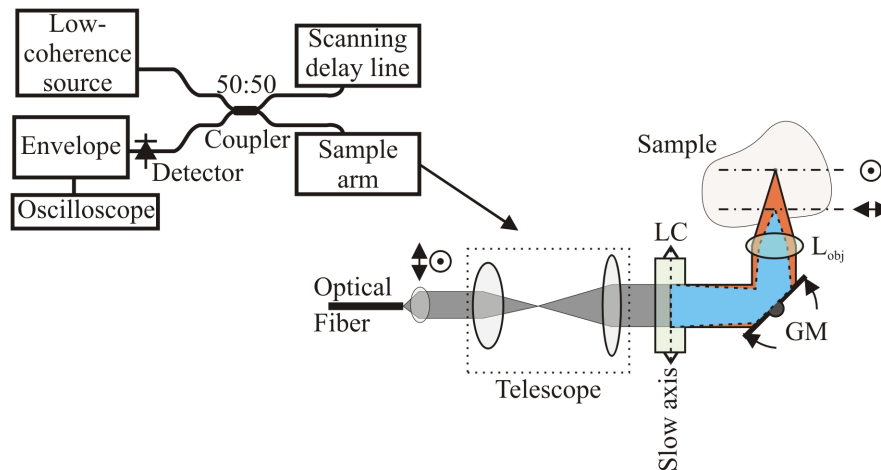


Fig. 1. Schematic diagram of the BOCR system showing the sample arm in detail. LC: liquid-crystal lens; GM: galvanometer-mounted tiltable mirror; L_{obj} : objective lens.

Marginal ray analysis

The refractive index of a medium can be calculated from the optical pathlength difference (OPD) between the two foci, i.e., the bifocal OPD, measured in the medium and in air. We use marginal ray analysis to derive the relationship between the refractive index and the bifocal OPD. The optical arrangement and relevant rays are shown schematically in Fig. 2. The sample is considered to be a medium of phase refractive index n and group refractive index n_g embedded in air with phase and group refractive indices of unity. The sample is

assumed to be separated from the sample-arm optics by a planar interface, as shown in Fig. 2. (The distorting effects of a nonplanar surface will be similar to those present in OCT and in other imaging techniques.) The sample is initially assumed to be homogeneous; the generalization to a heterogeneous medium is described subsequently. The geometry in Fig. 2 implies that the bifocal OPD in air, Δl , is given by

$$\Delta l = \frac{f_{\text{obj}}^2}{f_{\text{obj}} + f - s}, \quad (1)$$

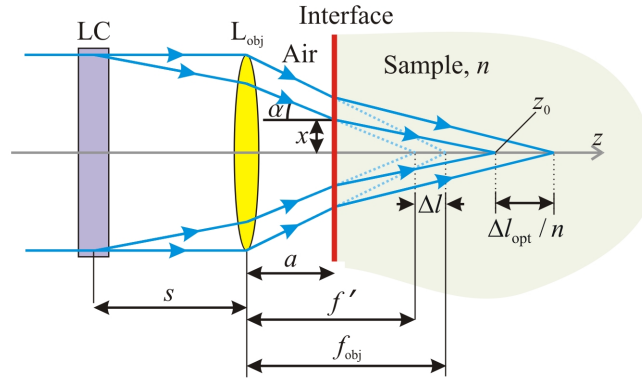


Fig. 2. Schematic diagram of the bifocal optical arrangement in the sample arm showing rays for the cases $n = 1$ (dashed) and $n > 1$ (solid).

where s is the distance between the principal planes of the liquid-crystal and objective lenses, and f and f_{obj} are their respective focal lengths. With the aid of Fig. 2, the bifocal OPD in the medium, Δl_{opt} , is found to be given by

$$\Delta l_{\text{opt}} = n_g \left\{ \frac{(f_{\text{obj}} - a)[(n^2 - 1)D^2 + 4n^2 f_{\text{obj}}^2]^{1/2}}{2f_{\text{obj}}} - \frac{(f' - a)[(n^2 - 1)(D')^2 + 4n^2 (f')^2]^{1/2}}{2f'} \right\}, \quad (2)$$

where D and D' are the $1/e^2$ beam diameters of the collimated and converging beams, respectively, at the input of the objective lens; a is the distance between the principal plane of the objective lens and the sample interface; and f' is the distance between the principal plane of the objective lens and the focal point in air of the converging beam. Equation (2) can be re-expressed in terms of the numerical aperture of the objective lens, NA , approximated as $\text{NA} \approx D/2f_{\text{obj}}$, to give

$$\Delta l_{\text{opt}} = n_g \left\{ (f_{\text{obj}} - a)[\text{NA}^2(n^2 - 1) + n^2]^{1/2} - \frac{(f_{\text{obj}} - a - \Delta l)[\text{NA}^2 f_{\text{obj}}^4 (n^2 - 1) + (nf \Delta l)^2]^{1/2}}{f \Delta l} \right\}. \quad (3)$$

To gain insight into the relationships between the parameters of the system, we can make several simplifications to Eq. (3) consistent with experimental conditions. Firstly, the focal length of the liquid-crystal lens is much greater than that of the objective lens and the lens separation, therefore $f \gg |f_{\text{obj}} - s|$. Using this fact and Eq. (1), we obtain the approximate relationship $f \Delta l \approx f_{\text{obj}}^2$, and substituting this relationship into Eq. (3) gives

$$\Delta l_{\text{opt}} \approx n_g n \left[1 + \text{NA}^2 \left(1 - \frac{1}{n^2} \right) \right]^{1/2} \Delta l. \quad (4)$$

Employment of a relatively low-numerical aperture objective lens implies $\text{NA}^2(n^2 - 1) \ll n^2$, and Taylor expanding to first order the term in parentheses in Eq. (4) gives

$$\Delta l_{\text{opt}} \approx n_g n \left[1 + \frac{1}{2} \text{NA}^2 \left(1 - \frac{1}{n^2} \right) \right] \Delta l. \quad (5)$$

Since the second term within the square parentheses in Eq. (5) is generally small, this result is in close agreement with $\Delta l_{\text{opt}} = n^2 \Delta l$ as used by Schmitt *et al.* [21]. Equations (3)-(5) show that the ratio $\Delta l_{\text{opt}} / \Delta l$ depends primarily on the refractive index of the sample and the effect of the other parameters of the system, including a and f , is small.

Equation (3) was used for computation of the refractive index from the experimental data under the assumption that the group and phase refractive indices are equal, which implies negligible variation in the refractive index over the wavelength range of interest. This assumption, also made in other interferometric schemes [14-17], implies a measurement accuracy on the order of 1%, depending on the sample [14]. Given the refractive index of biological samples is known to vary over the range 1.35-1.7 [1], this accuracy should be sufficient for most *in vivo* applications.

The preceding analysis shows that a single measurement of Δl_{opt} is sufficient to determine the refractive index at a given location in a sample provided Δl is predetermined and the system parameters are known or the system has been calibrated against a known standard. We now consider extending the method to a heterogeneous medium, continuing with the assumption that phase and group refractive indices are equal. For *in vivo* measurements, it is generally not practical to move the sample in order to scan the measurement location. Here we consider two methods of measuring the refractive index versus axial position that do not require movement of the sample.

The first method performs axial translation of a fixed bifocal OPD through axial translation of the objective lens. This translation is equivalent to variation of the parameter a shown in Fig. 2, provided this variation is small compared with the value of f so that there is negligible variation in the numerical aperture of the converging beam. This method has the disadvantage that the translation of the objective is usually slow. The measurement of $\Delta l_{\text{opt}} / \Delta l$ yields the local refractive index in the heterogeneous sample, independent of a as long as $f \gg |f_{\text{obj}} - s|$ is satisfied. The axial resolution is determined by the bifocal OPD. Importantly, the method enables a ‘snapshot’ measurement to be taken at any location, independent of other measurements.

The second method relies on changing the lens power, $1/f$, of the liquid-crystal lens, which, in effect, axially translates the confocal gate nearest the surface while the other is kept at a fixed location, thus, systematically varying the bifocal OPD. This method has the advantage that the translation does not involve mechanical inertia and has the potential to be much faster than the scanning-objective method. To proceed with a mathematical description of this method, we first explicitly define a refractive index, $n(z)$, which depends on the axial distance z . The physical location of the scanned focal point in the medium, z_0 , is related to the off-axis displacement of the marginal ray at the interface, x , its angle α with respect to the axis, and the refractive-index variations in the medium, by the equation

$$x = \int_0^{z_0} \frac{\sin \alpha}{\sqrt{[n(z)]^2 - \sin^2 \alpha}} dz, \quad (6)$$

where z_0 , x and α are shown in Fig. 2. We explicitly define the optical distance in the medium as z_{opt} , substitute the differential relationship $dz_{\text{opt}}/dz = n(z)$ and the approximation $\sin \alpha \approx \text{NA}$ into Eq. (6), then differentiate with respect to f to obtain the following result:

$$\left. \frac{dx}{df} \right|_{z=z_0} = \frac{\text{NA}}{n(z_0)\sqrt{[n(z_0)]^2 - \text{NA}^2}} \left. \frac{dz_{\text{opt}}}{df} \right|_{z=z_0}. \quad (7)$$

The left-hand side of Eq. (7) and NA are known and entirely independent of the medium. The factor dz_{opt}/df is measured directly (*i.e.*, $dz_{\text{opt}}/df = -d(\Delta l_{\text{opt}})/df$). Hence, the value $n(z_0)$ can be determined at any axial distance and, therefore, an axial refractive index profile can be generated.

The axial resolution is now determined by the widths of the coherence-scanned confocal gates rather than by their separation. The transfer function of a coherence-scanned confocal gate $I(l_r)$ is the convolution of the OCT source autocorrelation function $S(\Delta l_i)$ with the axial sample reflectivity $R(l_s)$ modified by the axial response function of the confocal optical system of the sample arm $h(l_s)$ [22], and given by

$$I(l_r) \approx \int_0^{\infty} \sqrt{R(l_s)h(l_s)} S(\Delta l_i) dl_s, \quad (8)$$

where $h(l_s) = h_1(l_s - l_{c1}) + h_2(l_s - l_{c2})$, h_1 and h_2 are the axial response functions of the two confocal gates, l_{c1} and l_{c2} are the positions of the peak values of h_1 and h_2 , respectively, $\Delta l_i = l_r - l_s$ is the optical pathlength difference, and l_r and l_s are the lengths of the reference and sample arms, respectively.

3. Experiment

To test the technique, an experimental setup based on a fiber-optic OCT system was constructed, equivalent to the schematic in Fig. 1. The main subsystem comprises a low-coherence scanning interferometer. The interferometer was illuminated with polarized light from a superluminescent diode with mean wavelength of 980 nm and 3-dB bandwidth of 28 nm corresponding to an axial resolution of 16 μm in air. The scanning optical delay line comprises a frequency-domain, folded grating-lens-and-tilted-mirror configuration operated off axis and in double pass [23]. The grating has 360 lines/mm and the lens is a 60-mm focal length, infrared achromatic doublet. The mirror is 30 mm in diameter and was angle-scanned via a galvanometer at 500 Hz, which enables an acquisition rate of four frames-per-second. Polarization controllers were placed in both the reference and sample arms, which enabled the balance of power between each focus in the sample arm to be adjusted. The sample arm comprises, in sequence, a liquid-crystal lens, galvanometer-based mirror, and objective lens. The liquid-crystal lens (OKO Technologies, Inc.) is used as the means to create two foci in the sample. It comprises a 25- μm -thick nematic liquid-crystal layer sandwiched between two plane parallel glass plates, each of which has a set of transparent annular electrodes on its outer surface. Application of an *ac* voltage to the electrodes randomizes the orientation of the pre-oriented nematic liquid crystal. The annular configuration results in the randomization being strongest at the edge and tailing off towards the center of the device. The resultant radial refractive-index gradient produces a lensing effect on light polarized along the slow axis of the device, *i.e.*, along the pre-orientation axis. The focus of the lens can be adjusted over the range 0.6 m to infinity, and requires 0.5 s to be reconfigured. This reconfiguration time is too slow for many dynamic applications, but is adequate to demonstrate the principle here. The galvanometer-mirror was employed for lateral scanning. The objective lens has a

focal length of 10 mm and a numerical aperture of 0.35. The $1/e^2$ diameter of the beam incident on the liquid-crystal lens was measured via a scanning slit to be 6 mm. The aperture of the liquid-crystal lens truncated the beam diameter to 5 mm. This reduced the effective numerical aperture of the objective lens to 0.25. The transverse resolution of the setup was estimated to be 5 μm . The total power delivered to the sample was 0.4 mW. At the output of the interferometer, the signal was photodetected and its envelope was determined using a logarithmic demodulator and subsequently transferred to a personal computer for display and storage.

3.1 Calibration procedure

Accurate determination of the refractive index requires accurate determination of the relevant parameters in Eq. (3), particularly f and Δl (or simply Δl if the approximation of Eq. (4) is to be used). We measured f via a scanning slit to calibrate the liquid-crystal lens at a wavelength of 980 nm. Δl was set to a nominal value in the range 70-225 μm and its exact value determined prior to each measurement session. This determination was initially performed by axial translation of a mirror through the two foci in air [19]. However, this procedure proved to be time consuming and prone to artefacts stemming from the mirror alignment. To overcome these shortcomings, an alternative calibration procedure was adopted. A measurement of Δl_{opt} in a homogeneous sample of known refractive index was performed, from which the required value of Δl could be obtained from Eq. (3). We chose water as a suitable sample [24], to which was added 0.013% w/v of 310-nm-diameter polystyrene spheres to obtain sufficient scattering. The polystyrene spheres, as well as any impurities in the water, could slightly alter its refractive index. To eliminate this source of systematic error, we determined the refractive index of the suspension by using low-coherence interferometry to scan a 1-cm pathlength cuvette with and without the suspension present [13]. To enable detection of all interfaces of the cuvette, a long-range low-coherence interferometry system was employed operating at a longer wavelength of 1310 nm [25]. Using it, we obtained a value of 1.321 ± 0.003 for the water suspension, which is in good agreement with the reported value of 1.323 of pure water [24]. (The quoted error is the standard deviation of five measurements.) The formula provided in Ref. 24 was used to extrapolate the measured value to the 980-nm wavelength range used subsequently in experiments, and gave a value of 1.326. This sample was then used to precisely determine Δl at the commencement of each experiment.

3.2 Measurement procedure

For samples in liquid form, several droplets were placed on a glass cover slip, which was located in the sample-arm beam. For human skin *in vivo*, a volunteer lightly pressed the volar side of the thumb against a glass cover slip. By inspection, the two foci were manually adjusted to lie within the sample. The lateral scan was activated and cross-sectional (B-mode) OCT images of the sample were acquired.

The OCT images were used to create several video clips. Unless specified otherwise, each video frame corresponds to a successive displacement of the objective lens along the optical axis (the first method described in Section 2). At each axial position of the objective lens, either 60 or 234 frames (256 lateral \times 128 axial pixels) were acquired, depending on the experiment, and averaged to obtain a video frame. (The averaging was carried out to enhance image quality for viewing purposes but the bifocal gate was readily observed at four frames-per-second without averaging.) The objective lens was then repositioned and the acquisition and averaging procedure was repeated. Finally, all frames were used to form a video clip. No correction was made in the video clips for the logarithmic compression of the demodulated OCT signal. The images so-acquired may be described as conventional OCT images modulated by a strong bifocal transfer function, which can be readily visualized in the case of a scattering homogeneous medium. Figure 3(a) presents a video clip of a typical bifocal

cross-sectional image recorded in Intralipid aqueous solution. The motion of the two confocally-gated peaks in the axial direction is clearly observed. The signal-to-noise ratio of a video frame in Fig. 3(a) was 42 dB and in an unaveraged OCT frame was 19 dB.

To accurately determine the refractive index, all 128 axial scans of a 60 (or 234)-frame-average cross-sectional image were logarithmically decompressed. A 256-sample average axial profile obtained from the 128 axial scans and its theoretical fit are shown in Fig. 3(c). The theoretical fit is based on the square root of the expression in Eq. (8) in order to account for the presence of speckle, since the sum of signals from N scatterers scales with \sqrt{N} . The bifocal OPD in each axial profile was determined either by fitting a fourth-order polynomial to each peak and measuring the separation between the fitted maxima; or by performing a least-squares fit of the theoretical transfer function (Eq. (8)) to the experimental data with the separation of the two confocal gates as the fitting parameter. The resulting Δl_{opt} was used to compute the refractive index using Eq. (3). The average value, whenever it is specified below, was calculated from the set of 128 values.

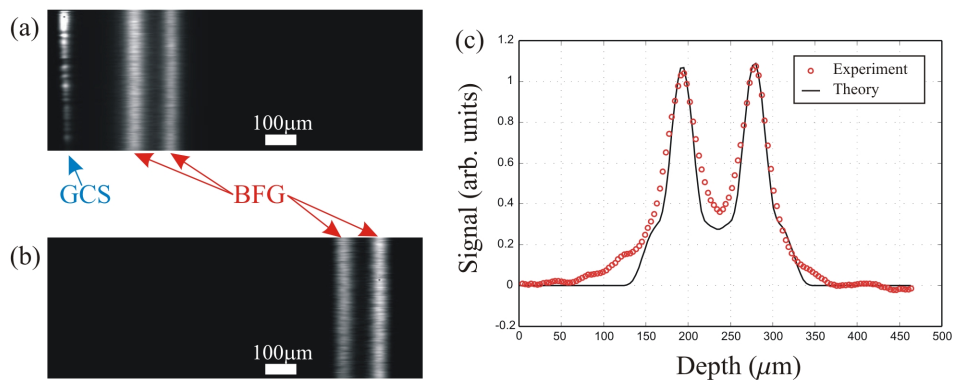


Fig. 3. (a), (b) (773 KB) Video clip (not real time, 234 OCT frames per video frame) of shifting the bifocal gate through an aqueous solution of Intralipid. Separate frames are shown in (a) and (b). GCS, glass cover slip surface; BFG, Bifocal gate signal. Scale bars represent optical pathlength. (c) Average axial profile from the images in (a) and (b), and its theoretical fit.

3.3 Sample preparation

We studied five samples: (1) a homogeneous Intralipid aqueous solution; (2) a homogeneous, high-refractive index suspension of zinc-oxide (ZnO) nanoparticles in paraffin oil; (3) a heterogeneous sample comprising a layer of ZnO nanoparticles in paraffin oil and a layer of Intralipid aqueous solution; (4) a set of varying-refractive index aqueous solutions of Intralipid and sugar, and (5) the volar side of a human thumb *in vivo*.

The Intralipid solution was prepared by dilution of 20% Intralipid solution in distilled, de-ionized water in volume proportion of 1:9.

The ZnO suspension was prepared from ZnO nanoparticles (Advanced Nano Technologies Pty Ltd), which were synthesized by mechanochemical processing [26] resulting in a mean particle size of ~30 nm and a very low degree of agglomeration. The ZnO nanoparticles are coated with stearic acid and dispersed in a 50:50 v/v mixture of caprylic/capric triglyceride and paraffin oil, yielding a concentration of 18% by weight. This mixture was diluted in paraffin oil in proportion of 1:20 to give an appropriate signal level. The refractive index of pure ZnO is approximately 1.93 at 980 nm [27].

The two-layer sample comprised a layer of the ZnO suspension retained by a small ring placed on the top of a cover slip. The layer was covered by a 13- μm -thick plastic membrane and several droplets of Intralipid solution were placed on top of the plastic membrane.

The varying-refractive index sample comprised a set of Intralipid solutions to which sucrose syrup was added in the volume ratio of 1:9. The sucrose syrup concentration in the solutions varied from 0 to 67% w/v.

To assist with adequate penetration, the volar side of the volunteer's index finger was prepared by being soaked in a warm soapy bath for 15 minutes, and subsequently allowed to dry in air for a further 15 minutes prior to imaging.

4. Results

In this section, we present measurements of the samples described above based on the objective scanning method, as well as demonstrate variation of the bifocal optical pathlength using the liquid-crystal lens.

To validate the accuracy of the technique and test for any position-dependent bias, measurements were first made on a homogeneous sample of Intralipid, as presented in Fig. 3(a). Figure 4 shows the corresponding refractive index tomogram. The standard deviation of the refractive-index measurements is 0.007. The figure confirms that some small systematic variation is present. The outer edges of the x-scan have slightly higher refractive index than the inner regions. This is most likely caused by lens aberrations that lead to a systematic increase in $\Delta l_{\text{opt}} / \Delta l$ with the x-scan beam-angle.

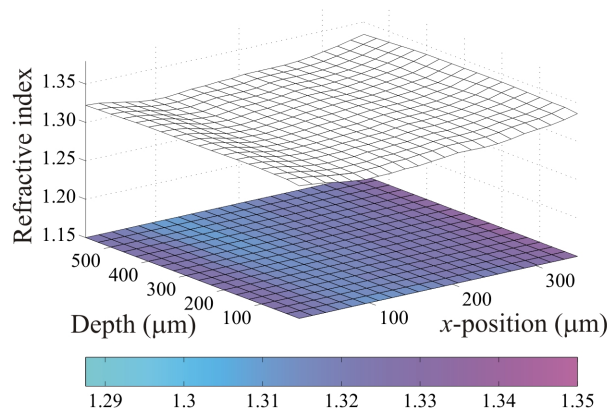


Fig. 4. Refractive-index tomogram (combined mesh and color plots) of a homogeneous Intralipid aqueous solution (corresponding to Fig. 3(a), (b)).

To demonstrate the basic feasibility of the bifocal optical pathlength-scanning method outlined in Section 2, we recorded a video clip in which each frame corresponds to an increased lens power setting of the liquid-crystal lens. Setting the focal point at a location well into the Intralipid solution and increasing the lens power successively shifts one gate towards the surface of the Intralipid aqueous solution. The results are shown in Fig. 5. The first frame of the video clip shows that with the liquid-crystal lens switched off no bifocal separation is seen. As the lens power is increased, the gated signal gradually splits until the bifocal gate is clearly observed at the maximum lens power of the liquid-crystal lens, $1/f = 1.67$ diopters. The scan range and reconfiguration time of the liquid-crystal lens are limited and so this method was not used for measurements of the samples.

To assess the suitability of BOCR for biomedical applications, it is important to determine its accuracy in turbid media over the range of refractive indices that are encountered in biological tissues. The ZnO suspension is a turbid sample with a refractive index at the high end of the relevant range. We obtained a value of 1.48 ± 0.01 , which marginally exceeds the tabulated value of 1.4668 ± 0.0002 for pure paraffin oil [28]. The

discrepancy is at least partly attributable to the addition of ZnO and caprylic/capric triglyceride oil.



Fig. 5. (1157 KB) Video clip (not real time, 234 OCT frames per video frame) of the scan of one focus of the bifocal gate. An indicator in the top left corner gives the focal length of the liquid-crystal lens. Scale bar represents optical pathlength.

Many tissues, e.g., skin [2], are heterogeneous, layered media in which each layer is characterized by a different average refractive index. A video clip of a bifocal-gate scan through the heterogeneous sample is presented in Fig. 6. The figure presents two montaged

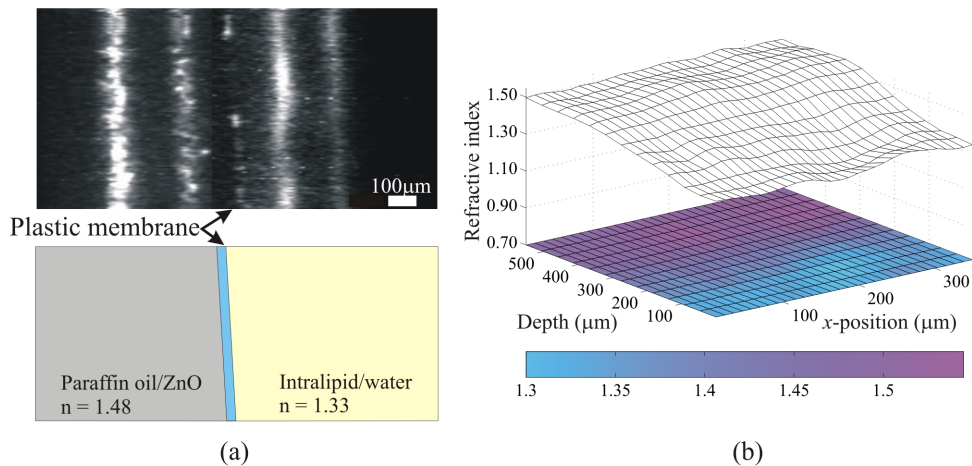


Fig. 6. (a) (517 kB) Video clip (not real time, 60 OCT frames per video frame) of the bifocal-gate scan and schematic diagram of the two-layer sample. (Two montaged frames are shown in the figure and the scale bar represents optical pathlength). (b) Combined mesh and color plots of the refractive index determined from the data set displayed in (a).

frames in which the bifocal gate in each layer is shown. The difference in gate widths is clearly observed. In the video clip, the bifocal gate is initially situated in the high-refractive index ZnO/paraffin oil medium and moves towards the lower-refractive index Intralipid solution. The particularly strong signal evident during the transition from the first to the second layer is caused by the plastic membrane. The refractive index tomogram for this sample is presented in Fig. 6(b). The change in refractive index in passing from one layer to another is clearly observable. To determine the refractive index within a layer, an average over sixteen lines in the transverse dimension was computed. The results are plotted versus axial position in Fig. 7. The extended transition region between the two layers seen in Fig. 7 is primarily governed by the impulse response (optical path difference) of the bifocal gate.

Equation (8) was used to fit a curve to the experimental data, which yielded a bifocal-impulse response (physical width) of $140\ \mu\text{m}$ in the paraffin layer, in agreement with the expected value based on the preliminary determination of Δl . It is interesting to observe in the video that the speckle pattern of each layer is different. The speckle due to the suspension in paraffin oil has a coarser, more granular appearance than the speckle in the Intralipid solution. There exist several indications in the literature that the spatial and temporal structure of speckle patterns reflects the scattering and dynamic properties of the sample [29].

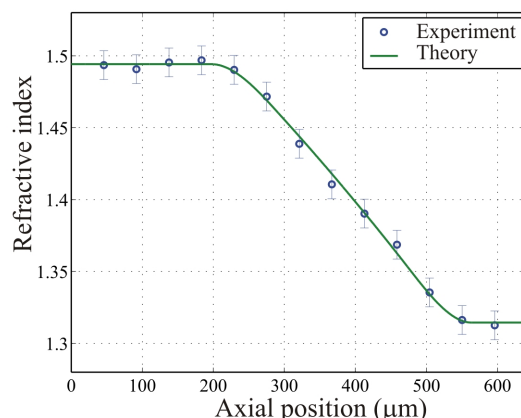


Fig. 7. Average refractive index versus axial depth of the heterogeneous sample.

To demonstrate the sensitivity of the technique to variations in refractive index, we examined a range of Intralipid solutions into which varying concentrations of sugar (sucrose) had been dissolved. The refractive index of sucrose solutions versus concentration has been tabulated and is widely used in food production, agriculture, and medicine [30]. The results of these measurements and their comparison with the tabulated data are presented in Fig. 8. Figure 8(a) is a video clip of the bifocal OPD variation in Intralipid solution versus sucrose concentration. The bars in the figure show the corresponding sucrose concentration, C , (left) and the computed refractive index, n , (right). The bifocal OPD can be seen to increase as the sucrose concentration increases. Figure 8(b) presents a plot of the computed and tabulated [30] refractive indices versus sucrose concentration. The error bars on the computed data are equivalent to one standard deviation of the measured bifocal OPD. The experimental data points were fitted using Eq. (8). The fitted curve is plotted in Fig. 8(b) as a dashed line. Note that we present results for the refractive index at 980 nm, whereas, the tabulated values (blue dots) apply to the visible wavelength range. There is a separation between the two curves and this separation increases with sucrose concentration. The separation is attributable to the refractive index of water being higher in the visible than in the infrared and the increase with concentration is attributable to the slightly higher dispersion of sucrose.

To demonstrate the main target of BOCR, the refractive-index tomography of biological tissue *in vivo*, Fig. 9(a) is a video clip of the bifocal OPD variation in a thick stratum corneum layer on the volar side of the index finger, and Fig. 9(b) is the measured refractive-index tomogram. The depth axis records the distance from the skin surface to the midpoint between the gates. At the scan endpoints, both gates were located in the stratum corneum. Figure 9 shows the refractive index gradually decreases from a maximum value of 1.56 adjacent to the air/skin interface to a value of 1.34 adjacent to the stratum corneum/epidermis interface. The refractive-index dependence is in agreement with the results of Casper *et al.* for the water content in thick stratum corneum obtained from Raman spectroscopy [31]. The variation in refractive index is assumed to depend on the relative concentrations of water (low index) and

protein/lipids (high index), thus, the dryer surface has a greater refractive index than the lower part.

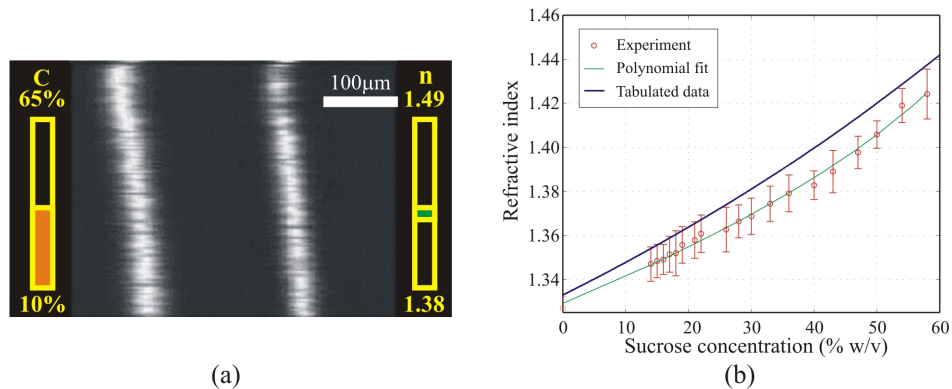


Fig. 8. (a) (313 kB) Video clip (not real time, 60 OCT frames per video frame) of the bifocal gate scan versus sugar concentration in the Intralipid aqueous solution. Scale bar represents optical pathlength. (b) Plot of sucrose concentration versus the measured average refractive index of the sample.

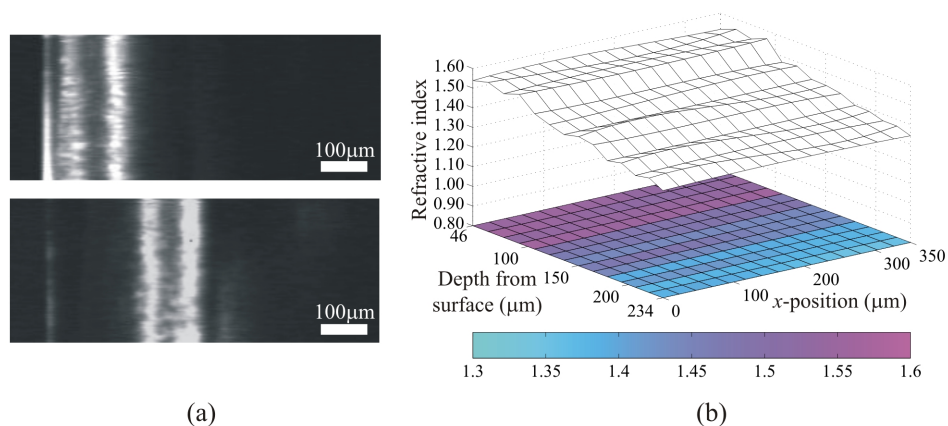


Fig. 9. (a) (358 kB) Video clip (not real time, 234 frames per video frame) of the bifocal gate scan in human thick stratum corneum *in vivo*. (Two frames are shown in the figure and the scale bars represent optical pathlength.). (b) Refractive-index tomogram calculated from (a).

5. Discussion

It is worthwhile commenting on several issues before concluding. When axial translation of the fixed bifocal OPD (objective scanning) is employed, BOCR is an intrinsically differential method in which each measurement does not rely on previously measured values and, thus, there is no requirement for iteration [2,14,15]. It is possible to operate in a non-scanning, static ‘snapshot’ mode, whereby an independent measurement can be made at a chosen location in the sample. In this mode of operation, the axial resolution is determined by the bifocal OPD, which can be traded off with measurement accuracy. The dependence of measurement accuracy on the bifocal OPD can be understood from the following. If n is varied with respect to Δl_{opt} in Eq. (5), we obtain for the uncertainty in n , defined as δn , the expression $\delta n \approx \delta(\Delta l_{\text{opt}})/2n\Delta l$, where $\delta(\Delta l_{\text{opt}})$ is the uncertainty in the bifocal OPD. This

expression shows that as Δl increases, δn decreases, all other things being equal. In our experiments on phantoms involving objective scanning, the bifocal OPD was deliberately set at a high value of approximately 140 μm in air, or greater, in order to well resolve the bifocal peaks. For the *in vivo* measurements in skin, a lower value of 102 μm in air was used to improve the axial resolution. For the alternative scheme we have proposed, in which one confocal gate is scanned while the other is held fixed, the axial resolution is set by the gate widths when the gates are well separated and so will always exceed the resolution obtained when both gates are scanned.

In general then, the axial resolution is limited by the axial response functions of the individual peaks. The peak axial response functions are a convolution of the confocal and coherence gates of the system. The experimental axial resolution (physical length) for the scan displayed in Fig. 5 was found to be 41 μm FWHM. With a modest increase in the numerical aperture to 0.45, the peak axial response could be reduced to 22 μm . Employing the Rayleigh criterion, the smallest bifocal OPD in air that could be employed would then be 17 μm . We note that these resolutions could be further improved by employing deconvolution. The above values compare favourably with the 30 to 50- μm axial resolution demonstrated in tissue by Knüttel *et al.* by using the focus-tracking technique [2]. It should be noted that Knüttel *et al.* employed a higher numerical aperture lens (0.45 versus effectively 0.25) and a shorter coherence gate width (8 μm versus 16 μm FWHM in air). In our case, we were limited by the available lens and source.

The polarization dependence of the liquid-crystal lens implementation of bifocal pathlength scanning implies sensitivity to the birefringence of the medium. It is straightforward to show that for birefringence δ the fractional error in the measured refractive index is given approximately by $(f_{\text{obj}} - a)\delta/n\Delta l$. Data on tissue birefringence is sparse, but indications are that maximum values lie in the 10^{-3} range [32]. With 50- μm resolution at a depth of 1 millimeter in tissue, such values would imply a worst-case error on the order of a few percent, which could be significant. This suggests that alternative non-polarization sensitive implementations could be preferable, or that caution should be exercised when probing tissue known to contain substances such as collagen, which are highly birefringent. Alternatively, the birefringence of the sample (ordinary and extraordinary refractive indices) could be determined by performing consecutive measurements in which the liquid-crystal lens orientation differs by 90 degrees.

An important issue affecting the accuracy of BOCR is speckle noise, also common to the focus-tracking techniques [15]. As seen from Figs. 3, 5, 6, and 8, speckle noise degrades the accuracy of the bifocal OPD measurement. We have ameliorated its effects by performing colocal or colateral averaging. Averaging comes at the expense of either slower acquisition speed, which should be, at least, on the sub-second scale to ensure motion-artefact-free measurements, or spatial resolution, which is restrictive and inappropriate for some heterogeneous samples. Our experiments have utilized modest optical power levels and resolution. Increases in both should lead to significant reductions in the averaging required to generate refractive-index tomograms with associated accuracies in the percent range. If this can be achieved while maintaining spatial resolution in the vicinity of 50 μm , then this level of performance should be adequate for many biomedical applications [1,14,15], including dynamic monitoring of uptake of substances in the skin, the progress of photodynamic therapy, assessment of burns, and tissue calcification.

6. Conclusion

We have presented an initial study of BOCR for refractive index tomography of turbid samples. The simultaneous creation of two foci in the sample and the measurement of the optical pathlength between them is a direct measure of the average refractive index over that pathlength in a sample, without the requirement for strongly reflecting surfaces. Because of its differential nature, BOCR is robust to variations in the parameters of the medium outside

the measurement volume. A key advantage of our technique in comparison with other focus-tracking approaches lies in its capability to take a 'snapshot' of the local refractive index of a heterogeneous sample without the need to perform an iterative procedure. Thus, there is the potential for avoidance of motion artefacts and for rapid *in vivo* refractive index tomography of turbid biological tissue. With improvements in scan speed and resolution, this feature may make feasible the study of dynamic processes.